Innovative quantitative analysis of left ventricular axis from cardiac SPECT images: XCAT phantom study and clinical validation

Fatemeh Salahshourinejad[1], Ahmad Keshavarz[1], Esmail Jafari[2,3], Majid Assadi[2,3]

[1]Electrical Engineerimg Department, Faculty of Intelligent Systems Engineering and Data Science, Persian Gulf University, Bushehr, Iran
[2]The Persian Gulf Nuclear Medicine Research Center, Bushehr University of Medical Sciences, Bushehr, Iran
[3]Department of Nuclear Medicine, Molecular Imaging and Theranostics, Bushehr Medical University Hospital, School of Medicine, Bushehr University of Medical Sciences, Bushehr, Iran

Corresponding author:
Dr. Ahmad Keshavarz
Electrical Engineerimg Department, Faculty of Intelligent Systems Engineering and Data Science, Persian Gulf University, 7516913817 Bushehr, Iran
E-mail: a.keshavarz@pgu.ac.ir

Running title: Left ventricular axis from cardiac SPECT images

ABSTRACT
Introduction: In this study, we aimed to evaluate the possibility of assessing cardiac abnormality using the left ventricular anatomical axis (LVAA) obtained from short-axis views of myocardial perfusion imaging (MPI).
Methods: To obtain LVAA, an ellipse was drawn around the outer wall of SPECT images from XCAT phantoms and patients. The best line was then drawn from the center of all the ellipses in the short-axis views called LVAA. Then, we defined two angles based on LVAA including Ө which is the angle created by LVAA with the x-axis, and Φ which is the angle created by LVAA with the z-axis.
Results: In this study, 94 cases were enrolled including 48 males (51%) and 46 females (49%) with a mean age of 65.65 ± 10.04. According to the results, there was a significant difference between the two obtained angles and the result of the scan ($p<0.05$). The ideal cut-off of Ө for an abnormal scan was 91.79 (AUC, 0.93; p=0.001) with the sensitivity of 98% and specificity of 80%.
Conclusion: It can be concluded that LVAA as a quantitative factor is significantly different between normal and abnormal MPS and can be used for the evaluation of MPI.

Keywords: Myocardial perfusion imaging; SPECT; Cardiovascular imaging; Left ventricular axis; [^{99m}Tc]Tc-MIBI

1

INTRODUCTION
The function of the left ventricle involves a complex interaction between different groups of muscle fibers oriented in various directions, including longitudinally, obliquely, and circumferentially. This results in a combination of the ventricle shortening in a circumferential manner, thickening of the heart wall in a radial direction, and shortening along its long axis [1, 2]. Research has shown that the displacement of the atrio-ventricular plane along the long axis is a significant factor in the pumping action of the left ventricle in healthy individuals as well as in those with diseased hearts. Furthermore, the long axis function influences myocardial function in unique ways, such as playing a role in left ventricular diastolic filling and facilitating the filling of the atria from the major veins. Dysfunction along the long axis has been observed as an early indicator of various pathological conditions [3]. Echocardiography, which assesses the longitudinal function, has demonstrated its ability to provide valuable prognostic information for a wide range of heart conditions [3]. Despite these distinctive characteristics, the assessment and reporting of long axis function are not commonly performed even during clinical Cardiovascular Magnetic Resonance (CMR) evaluations [4].

Myocardial perfusion imaging (MPI) [5] is a cardiovascular imaging method performed to diagnose coronary artery disease (CAD) in two phases following exercise and rest for evaluating the quantity and quality of blood supply to the myocardium at different angles and levels of the heart [6, 7]. Clinically, physicians have studied left ventricular SPECT images using various methods such as heart segment and converting it into a variable mesh model with parameters such as ejection fraction, stroke volume, wall thickness, and wall motion [8, 9]. These parameters are very useful in the diagnosis of heart attack, heart failure, and evaluation of the amount of living and surviving heart muscle [10, 11].

Unfortunately, one of the problems with SPECT images is that they are noisy and also have a low resolution [12, 13]. Therefore, it is difficult to extract quantitative measures [14, 15]. We run this novel project to develop basic principles based upon cardiac imaging methods, which has accomplished widespread clinical acceptance as a standard of care for patients with coronary artery disease. Hopefully, it might be to use as a surrogate in detection of cardiovascular problems especially ischemic disease in future studies. Furthermore, adding a quantitative measurement that can extract more information from these images will help the physician to be able to diagnose the disease more accurately. In this study, we aimed to evaluate the possibility of assessing the cardiac abnormality using the left ventricular anatomical axis (LVAA) obtained from short-axis views of MPI.

METHODS
Patients
In this retrospective study, 94 patients who underwent MPI from July 2020 to January 2021 were enrolled. The clinical history of patients was collected from medical documents. This was a registry-based retrospective study approved by our Institution Review Board.

Myocardial perfusion SPECT (MPS)
MPS was performed in one-day stress and rest phases. Following intravenous injection of 740 MBq [^{99m}Tc]Tc-MIBI, the image acquisition was performed after at least one hour for rest and at least 30 minutes for exercise or pharmacologic stress. The images were acquired from the right anterior oblique (RAO) to the left posterior oblique (LPO) in 32 projection (20 second/projection)

and 64×64 matrix using a dual-head gamma camera (Philips (ADAC) Vertex Plus) equipped with low energy-high resolution collimator. The energy window was set at 140±20%. Image reconstruction was performed using the ordered subset expectation maximization (OSEM) with the combination of four iterations and four subsets.

Two nuclear medicine physicians reviewed the images. Based on interpretation, the images were classified into normal scans and abnormal scans including both infarcted and ischemic myocardium.

Phantom study

Since SPECT images are noisy, we required laboratory images, so the XCAT Phantom was used. The integration of the four-dimensional XCAT phantom with the SIMIND Monte Carlo program provides a robust framework for simulating scintillation camera imaging and Single Photon Emission Computed Tomography (SPECT). The XCAT phantom, a sophisticated 4-D extended cardiac-torso model, offers a detailed representation of human anatomy and physiology. Its flexibility allows for the simulation of diverse physiological conditions, making it a valuable tool in nuclear medicine research. In this study, the XCAT phantom was employed to generate realistic laboratory images due to the inherent noise in SPECT images [16]. The phantom accommodates variations in gender, weight, height, body elongation, chest dimensions, and the presence or absence of breasts, ensuring a broad applicability to different patient demographics. The use of four phantoms at eight different time points throughout the cardiac cycle allowed for a comprehensive representation, and the average was considered for subsequent analysis[16]. The SIMIND Monte Carlo program served as a reliable tool for simulating scintillation camera imaging and SPECT [17]. This program accounts for the physical and geometrical characteristics of the camera system, making it a comprehensive forward projector in an iterative reconstruction algorithm. Specifically, SIMIND utilized a Maximum Likelihood Expectation Maximization (ML-EM) and Ordered Subsets Expectation Maximization (OSEM) reconstruction algorithm to estimate the source distribution and image data (Figure 1) [18]. In the simulation process, the XCAT phantoms were used as inputs to the SIMIND code. The parameters specified in the SIMIND software included an energy of 140.5 Kev for photons (matching technetium's energy), 32 shots, and $256 \times 256 \times 128$ matrices for both activity and attenuation maps. The cut-off energy for tracking photons was set at half of the initial photon energy (70 Kev). The output from SIMIND was then converted into SPECT images using the OSEM reconstruction algorithm [9]. Notably, the XCAT phantom was configured to simulate SPECT images with different activity distributions in various organs. It can accurately simulate cardiac activity, with relatively high and equal activity in all four chambers of the heart, along with abdominal activity, including the liver, gall bladder, esophagus, spleen, and specific activities of Tc-99m was set for male and female phantoms. The XCAT phantom could simulate 3D distribution of attenuation coefficients and emission radionuclide activity, offering a comprehensive approach to imaging simulation. [17, 18]. The synergistic use of the XCAT phantom and the SIMIND Monte Carlo program in this study allowed for the creation of realistic and diverse SPECT images. This methodology enhances the understanding of imaging processes, facilitating advancements in nuclear medicine research and contributing to the refinement of imaging techniques.

Image segmentation

Because this article was supposed to enclose the images of the myocardial short-axis views in an ellipse, these images must be segmented to find the edges of the images, so their segmentation is

necessary. We used the images of the stress phase for the segmentation and calculation of LVAA. Sub-Markov Random Walk (SMRW) [19] was applied for image segmentation. In this method, the user specifies the starting points of each image area that corresponds to a separate object in the image. The user labels each starting point. The SMRW marks all unlabeled points, then, calculates the probability of reaching each marked point from the starting point and finally, finds the highest probability. For this purpose, a vector is formed from which each element indicates the probability of reaching each of the areas separated by the user from the starting point to the label [20]. Finally, by separating the area that has the activity in heart, it creates the image needed for the next part, which is ellipse estimation. Therefore, an accurate ellipse estimation method is very critical for the estimation of the desired axis. Therefore, segmented images must be enclosed in an ellipse to obtain their centers [19].

Ellipse estimation method
The method of estimating the ellipse is to calculate the diagonal distance regression, in which the geometric error is minimized. The orthogonal distance is the distance between the data points and the ellipse. This is a cost function that occurs when independent Gaussian noise is assumed to be a data point and applied to the maximum probability estimate [21]. The cost function is based on the number of data points. For clarification, if the data point (m1, m2) is incorrect in the ellipse, this function should match Eq.1.

$$ax^2 + bxv + cv^2 + dx + ev + f = 0 \tag{1}$$

This equation is a general conic equation and depending on whether the discriminant $\Delta = b^2 - 4ac$ is negative, zero, or positive, it represents ellipses, parabolas, and hyperbolas, respectively. As a result, for a data point to satisfy an ellipse equation, the ellipse parameters must also satisfy the ancillary constraint $b^2 - 4ac < 0$.

Assume $\theta = [a, b, s, d, e, f]^T$ is the vector of parameters, $x = [m_1, m_2]^T$ is the vector of variables and $u(x) = [m_1^2, m_1 m_2, m_2^2, m_1, m_2, 1]^T$ is the vector of transformed data points. The equation of a conic can then be written as $\theta^T u(x)$.

The algebraic least-squares method could be used to determine how much a data point fails to satisfy the ellipse Eq.2.

$$\frac{\|\theta^T u(x)\|^2}{\|\theta\|^2} = \frac{\theta^T u(x) u(x)^T \theta}{\|\theta\|^2} \tag{2}$$

Where $\| \theta \|^2 = (\theta_1^2 + \cdots + \theta_6^2)^2$. As a result of this, the algebraic least squares (ALS) cost function is as follows:

$$J_{ALS}(\theta; x_1, x_2, \dots, x_N) = \frac{\sum_{n=1}^N \theta^T u(x_n) u(x_n)^T \theta}{\|\theta\|^2} = \frac{\theta^T M \theta}{\theta^T \theta} \tag{3}$$

Where $M = \sum_{n=1}^N \theta^T u(x_n) u(x_n)^T \theta$. Because it is so simple to minimize, the algebraic least-squares cost function is extremely common. This formula is written in the form of the Riley equation. The eigenvector associated with the least eigenvalue is the parameter vector $\hat{\theta}_{ALS}$ that minimizes the algebraic cost function. To find the estimate, all that is required is an

eigendecomposition. This is a simple and effective method to use. The ancillary constraint $b^2 - 4ac < 0$, on the other hand, is not applied in the procedure. This means that instead of an ellipse, the estimate $\hat{\theta}_{ALS}$ could be a hyperbola or parabola presented a change to the algebraic cost function that ensured an elliptical fit to address this constraint. It was called the Direct Ellipse Fit (DIR) [22, 23]. In this step, the edge points of the 8 images of the previous step are found. These are the input points of the ellipse estimation algorithm. Using these points, the circumferential ellipse is estimated. Then the center of the ellipse is found using Eq.4. The output sample of the ellipse is estimated and their centers are shown in figure 1C.

$$x = \frac{cd-be}{b^2-ac} \quad , \quad y = \frac{ae-bd}{b^2-ac} \tag{4}$$

3D axis estimation using cardiac centers
In this section, the points of the obtained elliptical centers were the input. The variance-covariance matrix of those points was obtained. This was the singular value decomposition (SVD) input matrix. Using the SVD function, the best line passing through these points was estimated [24].
SVD creates orthonormal bases for the null-space and range of a matrix explicitly. The columns of U corresponding to the non-zero elements of D cover the range. Columns of V corresponding to zero elements of D span the null space. SVD allows a rank decision (rank (A)) is the largest r s.t. Dr > 0). There is m - r singular vector on the left that corresponds to the singular value 0. There is n - r singular vectors on the right corresponding to the singular value 0.
SVD (x) returns the numeric unit matrix U and V with columns containing single vectors and a diagonal matrix D containing single values. The matrix satisfies the condition A = U × D × V`, where V` is the hermetic transposition (different conjugate of transposition) of V(28). SVD does not compute single symbolic vectors; therefore, the input matrix X must be converted to floating-point numbers. The proper direction of the line is proportional to U (: , 1). By converting U to the polar coordinates, the output is the angles Θ and Φ (R^2 coefficient of determination = (variance) / (total variance)) [25]. At this point, the output Θ is a spatial angle created by the three-dimensional line estimated with the x-axis. To compare the results of the algorithm, all steps of the algorithm had been performed on XCAT phantom images. Figure 2 shows an example of image segmentation and achievement of LVAA with angles for abnormal scan and normal scan.

Classification
Support vector machine (SVM) [26] is a method of observational classification based on statistics. This classifier's main purpose is to determine the meta-page that maximizes the margin between the two classes as a decision level. SVM classifier separates two classes by a hyperplane within the N-dimensional space. The discriminant function of the SVM classifier is defined as

$$f(\mathbf{Y}_j) = sign(\mathbf{W}^T.\mathbf{Y}_j + b) \tag{5}$$

where b could be consistent and **W** maybe a vector with real values. In case, if data cannot be separated linearly, discriminant function is defined as

$$f(\mathbf{Y}_j) = sign(\mathbf{W}^T.\Phi(\mathbf{Y}_j) + b) \tag{6}$$

Where $\Phi(\mathbf{Y_j})$ is a function to map the $\mathbf{Y_j}$ into a higher dimensional feature space. Ordinarily nonlinearly distinguishable information is mapped into higher dimensional including space utilizing bit capacities [27]. Hence, discriminant work can be altered as takes after:

$$f(\mathbf{Y_j}) = sign(\sum_i \alpha_i K(\mathbf{Y_j}.\mathbf{Y_i}) + b) \qquad (7)$$

Where $\mathbf{Y_i}$ and α_i are ith support vector and its corresponding weight respectively. $K(.,.)$ is the kernel function. One of the kernels that are commonly used in practical applications is a Radial Basis Function (RBF) is given as in Eq.6.

$$K(\mathbf{Y_j}.\mathbf{Y_i}) = \exp(-\parallel \mathbf{Y_j} - \mathbf{Y_i} \parallel)^2 \qquad (8)$$

For classification, we considered 70% of cases as train and 20% as the test with 100 times repeat. Three models were evaluated to predict the result of the scan including the results of both angles as model 1, the results of Θ as model 2, and the results of Φ as model 3. In the end, precision, recall, and receiver operating characteristic (ROC) curves for the determination of the area under the curve (AUC) were obtained as output.

Statistical analysis
IBM SPSS Statistics for Windows, version 21 (IBM Corp., Armonk, N.Y., USA) was used for data analysis. Continuous variables were presented as mean ± SD, and categorical variables were presented as numbers and percentages. In addition, the T-test was used to the assessment of the difference between groups. Finally, ROC curve analysis was used to determine the cut-off value and AUC. P-values less than 0.05 were considered statistically significant.

RESULTS
Phantom study results
Table 1 shows the results of the algorithm using the XCAT phantom and its SPECT simulation images in an average of eight times. The results indicated that there was no significant difference between cardiac Φ and Θ of phantom and reconstructed SPECT images obtained from the phantom (p>0.05).

Patient study
The results of this algorithm had also been tested on real MPS data in 94 cases that underwent MPI including 48 males (51%) and 46 females (49%) with a mean age of 65.65±10.04. Of 94 cases, 53 (56.4%) showed normal scans while 41 cases (43.6%) showed abnormal scan results. Baseline characteristics of patients are presented in Table 2. According to the results, there was a significant difference between the two obtained angles and the result of the scan (p<0.05). The mean of Θ for the abnormal group and normal group were 130.62±25.44 and 78.86±24.68 (p=0.001) and for Φ were 36.90±10.95 and 42.73±9.68 (p=007), respectively. According to the receiver operating characteristic (ROC) curve analysis with the area-under-the-curve (AUC), the ideal cut-off of Θ for an abnormal scan was 91.79 (AUC, 0.93; 95%CI, 0.88-0.99; p=0.001) with the sensitivity of 98% and specificity of 80%. In addition, the ideal cut-off for Φ for a normal scan was 44.22 (AUC, 0.68; 95%CI, 0.57-0.79; p=0.003) with a sensitivity of 56% and specificity of 81% (Figure 3).

There was no significant relationship between the two angles with age, sex, hypertension, and diabetes (p>0.05).

To classify these data with SVM, 66 cases were used as training set and 28 cases were used as test, which have been selected randomly. The recall was obtained 0.9164 ± 0.1007, 0.8973 ± 0.1015, 0.6082 ± 0.1766 for model 1 ($\Theta+\Phi$), model 2 (Θ), and model 3 (Φ), respectively. The precision was obtained 0.7805 ± 0.0782, 0.7697 ± 0.0952, 0.4310 ± 0.0702 for model 1 (Θ and Φ), model 2 (Θ), and model 3 (Φ), respectively. Furthermore, AUC was obtained 0.9351 ± 0.0413, 0.9292 ± 0.0582, 0.6232 ± 0.0758 for model 1 (Θ and Φ), model 2 (Θ), and model 3 (Φ), respectively (Figures 4 & 5).

DISCUSSION

In the last decades, several efforts have been introduced for application of quantitative parameters in medical imaging modalities for faster and more accurate interpretation. For MPI, various quantitative parameters are applied such as quantitative polar map which displays the extent, and severity of myocardial perfusion defects [28]. Total perfusion deficit (TPD) is another quantitative parameter of overall magnitude of hypoperfusion [29]. In addition, segmental perfusion scores which divides cardiac territories into 17 segment and each segment is scored 0-5 based on uptake (0 = normal; 1 = mildly abnormal; 2 = moderately abnormal; 3 = severely abnormal; 4 = absent), then based on the scores, defect severity is calculated [30]. Various validation studies have been performed for these parameters [31-33].

In this study, we tried to introduce a new quantitative parameter for the interpretation of MPI by using two angles obtained from LVAA. We indicated that there is a significant difference between these angles defined as theta (Θ) and phi (Φ) with the result of the scan, which Θ was significantly higher in abnormal scan compared to normal scan and Φ was significantly higher in normal scan compared to abnormal scan. It has been shown that Θ can diagnose the abnormal scan with sensitivity and specificity of 98% and 80%, respectively. In addition, Φ with sensitivity and specificity of 56% and 81% can diagnose normal scans. Therefore, they can be used for the interpretation of MPI, quantitatively. In addition, there was no significant relationship between these angles with sex, age, diabetes, and hypertension.

In this study, we have demonstrated the possibility of quickly assessing the Left Ventricular Axis of the Heart using SPECT Images - as a substitute for LV long axis function - during routine gated cardiac SPECT protocol. To our knowledge, this is the first evidence of the diagnostic value of assessing LV long axis function using universally obtained cardiac SPECT images.

The function of the long axis is essential for the mechanics of the heart. Firstly, it helps with ventricular ejection by decreasing the size of the long axis left ventricle cavity. Secondly, during early diastole, the energy stored during systole creates suction in the ventricle, which is crucial for quick filling of the ventricle at low pressures in a healthy heart [2, 34].

The assessment of left ventricular long axis function using echocardiography has demonstrated its predictive value for negative cardiovascular outcomes in various conditions, such as atrial fibrillation, post-myocardial infarction, heart failure, and tetralogy of Fallot [35]. Recently, there has been significant interest in the prognostic potential of echo-derived global longitudinal strain, which has been found to forecast a range of adverse outcomes in different populations, including acute myocardial infarction, ischemic cardiomyopathy, heart failure (with reduced or preserved ejection fraction), aortic stenosis, tetralogy of Fallot, amyloidosis, post-heart transplantation, and post-anthracycline therapy [36]. Additionally, echo global longitudinal strain has been shown to independently predict the development of atrial fibrillation in a community-based cohort [37].

Korosoglou et al. utilized CMR to demonstrate that strain encoded magnetic resonance imaging (SENC) offered additional predictive value for patients undergoing dobutamine stress CMR [38]. More recently, Buss et al. showed that left ventricular longitudinal strain, evaluated using specialized CMR feature tracking software, independently predicts survival in dilated cardiomyopathy [39]. However, the analysis of strain using CMR has traditionally relied on specialized software, leading to limited adoption of these techniques in clinical practice.

This study is conducted at a single center and is observational in nature, thus it possesses the limitations adherent to this type of study design. Therefore, despite the adjustment for various clinically relevant factors, it is probable that some degree of residual confounding still exists. Our study had some drawbacks. First, we reported the primary results of our designed algorithm in the stress phase and, therefore, for better decision, the result of the rest phase should be added. Second, for more accurate result, the relationship between cardiac defect intensity and the variation in LVAA should be evaluated. In addition, we tried to outline the mechanism and influencing factors of LVAA with the anticipation of the routine application of these measurements in clinical practice. However, in what approach this information will be of use in clinical scenarios remains unclear. We await the day when such quantitative measurements are recognized as a new assessment of cardiac function. Verification of such data to large groups of patients who also have gold standard outcome measures is highly required.

CONCLUSION
It can be concluded that LVAA as a quantitative factor is significantly different between normal and abnormal MPS and can be used for the evaluation of MPS. However, further studies are needed for its application in clinical practice.

REFERENCES
1. Sanderson JE. Left and right ventricular long-axis function and prognosis. Heart. 2008 Mar;94(3):262-3.
2. Carlsson M, Ugander M, Heiberg E, Arheden H. The quantitative relationship between longitudinal and radial function in left, right, and total heart pumping in humans. Am J Physiol Heart Circ Physiol. 2007 Jul;293(1):H636-44.
3. Hu K, Liu D, Herrmann S, Niemann M, Gaudron PD, Voelker W, Ertl G, Bijnens B, Weidemann F. Clinical implication of mitral annular plane systolic excursion for patients with cardiovascular disease. Eur Heart J Cardiovasc Imaging. 2013 Mar;14(3):205-12.
4. Schulz-Menger J, Bluemke DA, Bremerich J, Flamm SD, Fogel MA, Friedrich MG, Kim RJ, von Knobelsdorff-Brenkenhoff F, Kramer CM, Pennell DJ, Plein S, Nagel E. Standardized image interpretation and post processing in cardiovascular magnetic resonance: Society for cardiovascular magnetic resonance (SCMR) board of trustees task force on standardized post processing. J Cardiovasc Magn Reson. 2013 May 1;15(1):35.
5. Schuijf JD, Matheson MB, Ostovaneh MR, Arbab-Zadeh A, Kofoed KF, Scholte AJHA, Dewey M, Steveson C, Rochitte CE, Yoshioka K, Cox C, Di Carli MF, Lima JAC. Ischemia and no obstructive stenosis (INOCA) at CT Angiography, CT myocardial perfusion, invasive coronary angiography, and SPECT: The CORE320 Study. Radiology. 2020 Jan;294(1):61-73.
6. Peix A, Karthikeyan G, Massardo T, Kalaivani M, Patel C, Pabon LM, Jiménez-Heffernan A, Alexanderson E, Butt S, Kumar A, Marin V, Mesquita CT, Morozova O, Paez D, Garcia EV. Value of intraventricular dyssynchrony assessment by gated-SPECT myocardial

perfusion imaging in the management of heart failure patients undergoing cardiac resynchronization therapy (VISION-CRT). J Nucl Cardiol. 2021 Feb;28(1):55-64.

7. Brankov JG, Yang Y, Narayanan MV, Wermck MN. Motion-compensated 4D processing of gated SPECT perfusion studies. IEEE Nucl Sci Symp Conf Rec (2002). 2002 Nov;3:1380-4.

8. Kennedy JA, Israel O, Frenkel A. Directions and magnitudes of misregistration of CT attenuation-corrected myocardial perfusion studies: incidence, impact on image quality, and guidance for reregistration. J Nucl Med. 2009 Sep;50(9):1471-8.

9. Okuda K, Nakajima K, Saito H, Ito T, Kikuchi A, Yoneyama H, Shibutani T, Onoguchi M, Matsuo S, Hashimoto M, Kinuya S. P126 Texture analysis of myocardial perfusion SPECT with a digital cardiac phantom. Eur Heart J Cardiovasc Imaging. 2019 Jun 1;20(Supplement_3):jez147-014.

10. He X, Jia W, Wu Q, Hintz T. Description of the cardiac movement using hexagonal image structures. Comput Med Imaging Graph. 2006 Sep-Oct;30(6-7):377-82.

11. Shi P, Sinusas AJ, Constable RT, Ritman E, Duncan JS. Point-tracked quantitative analysis of left ventricular surface motion from 3-D image sequences. IEEE Trans Med Imaging. 2000 Jan;19(1):36-50.

12. Hosny T, Khalil MM, Elfiky AA, Elshemey WM. Image quality characteristics of myocardial perfusion SPECT imaging using state-of-the-art commercial software algorithms: evaluation of 10 reconstruction methods. Am J Nucl Med Mol Imaging. 2020 Dec 15;10(6):375-86.

13. Beekman FJ, Slijpen ET, Niessen WJ. Selection of task-dependent diffusion filters for the post-processing of SPECT images. Phys Med Biol. 1998 Jun;43(6):1713-30.

14. Fallahi B, Beiki D, Salehi Y, Emami-ardekani A, Fard-esfahani A, Aghahosseini F, Eftekhari M. Benefits of combined pharmacologic and submaximal exercise stress on sub-diaphragmatic activity in myocardial perfusion scintigraphy. Iran J Nucl Med. 2018;26(2):105-11.

15. Zaidi H, Hasegawa B. Determination of the attenuation map in emission tomography. J Nucl Med. 2003 Feb;44(2):291-315.

16. den Boer E, Wulff J, Mäder U, Engwall E, Bäumer C, Perko Z, Timmermann B. Technical Note: Investigating interplay effects in pencil beam scanning proton therapy with a 4D XCAT phantom within the RayStation treatment planning system. Med Phys. 2021 Mar;48(3):1448-55.

17. Comtat C, Bataille F, Michel C, Jones JP, Sibomana M, Janeiro L, Trebossen R. OSEM-3D reconstruction strategies for the ECAT HRRT. IEEE Symp Con Rec Nucl Sci. 2004;6:3492-6.

18. Cocosco CA, Netsch T, Se J, Bystrov D, Niessen WJ, Viergever MA. Automatic cardiac region-of-interest computation in cine 3D structural MRI. Int Congr Ser. 2004;1268:1126-31.

19. Dong X, Shen J, Shao L, Van Gool L. Sub-Markov Random Walk for Image Segmentation. IEEE Trans Image Process. 2016 Feb;25(2):516-27.

20. Golub GH, Reinsch C. Singular value decomposition and least squares solutions. Handbook for automatic computation: Volume II: Linear Algebra 1971 Apr. Berlin, Heidelberg: Springer Berlin Heidelberg. p. 403-20.

21. Fitzgibbon A, Pilu M, Fisher RB. Direct least square fitting of ellipses. IEEE Trans Pattern Anal Mach Intell. 1999 May;21(5):476-80.

22. Szpak ZL, Chojnacki W, van den Hengel A. Guaranteed ellipse fitting with a confidence region and an uncertainty measure for centre, axes, and orientation. J Math Imaging Vis. 2015 Jun;52:173-99.
23. Liang J, Li P, Zhou D, So HC, Liu D, Leung CS, Sui L. Robust ellipse fitting via alternating direction method of multipliers. Signal Process. 2019;164:30-40.
24. Lok UW, Song P, Trzasko JD, Daigle R, Borisch EA, Huang C, Gong P, Tang S, Ling W, Chen S. Real time SVD-based clutter filtering using randomized singular value decomposition and spatial downsampling for micro-vessel imaging on a Verasonics ultrasound system. Ultrasonics. 2020 Sep;107:106163.
25. Yuan X, Han L, Qian S, Xu G, Yan H. Singular value decomposition based recommendation using imputed data. Knowl Based Syst. 2019;163:485-94.
26. Mavroforakis ME, Theodoridis S. A geometric approach to support vector machine (SVM) classification. IEEE Trans Neural Netw. 2006 May;17(3):671-82.
27. Auria L, Moro RA. Support vector machines (SVM) as a technique for solvency analysis. DIW Berlin Discussion Paper No. 811, 2008 August. Available from: https://ssrn.com/abstract=1424949
28. Slomka P, Xu Y, Berman D, Germano G. Quantitative analysis of perfusion studies: strengths and pitfalls. J Nucl Cardiol. 2012 Apr;19(2):338-46.
29. Slomka PJ, Nishina H, Berman DS, Akincioglu C, Abidov A, Friedman JD, Hayes SW, Germano G. Automated quantification of myocardial perfusion SPECT using simplified normal limits. J Nucl Cardiol. 2005 Jan-Feb;12(1):66-77.
30. Tilkemeier PL, Cooke CD, Ficaro EP, Glover DK, Hansen CL, McCallister BD Jr; American Society of Nuclear Cardiology. American Society of Nuclear Cardiology information statement: Standardized reporting matrix for radionuclide myocardial perfusion imaging. J Nucl Cardiol. 2006 Nov;13(6):e157-71.
31. Ansari M, Hashemi H, Soltanshahi M, Qutbi M, Azizmohammadi Z, Tabeie F, Javadi H, Jafari E, Barekat M, Assadi M. Factors That impact evaluation of left ventricular systolic parameters in myocardial perfusion Gated SPECT with 16 frame and 8 frame acquisition models. Mol Imaging Radionucl Ther. 2018 Jun 7;27(2):55-60.
32. Ficaro EP, Fessler JA, Shreve PD, Kritzman JN, Rose PA, Corbett JR. Simultaneous transmission/emission myocardial perfusion tomography. Diagnostic accuracy of attenuation-corrected 99mTc-sestamibi single-photon emission computed tomography. Circulation. 1996 Feb 1;93(3):463-73.
33. Slomka PJ, Fish MB, Lorenzo S, Nishina H, Gerlach J, Berman DS, Germano G. Simplified normal limits and automated quantitative assessment for attenuation-corrected myocardial perfusion SPECT. J Nucl Cardiol. 2006 Sep;13(5):642-51.
34. Rangarajan V, Chacko SJ, Romano S, Jue J, Jariwala N, Chung J, Farzaneh-Far A. Left ventricular long axis function assessed during cine-cardiovascular magnetic resonance is an independent predictor of adverse cardiac events. J Cardiovasc Magn Reson. 2016 Jun 7;18(1):35.
35. Diller GP, Kempny A, Liodakis E, Alonso-Gonzalez R, Inuzuka R, Uebing A, Orwat S, Dimopoulos K, Swan L, Li W, Gatzoulis MA, Baumgartner H. Left ventricular longitudinal function predicts life-threatening ventricular arrhythmia and death in adults with repaired tetralogy of fallot. Circulation. 2012 May 22;125(20):2440-6.
36. Thavendiranathan P, Poulin F, Lim KD, Plana JC, Woo A, Marwick TH. Use of myocardial strain imaging by echocardiography for the early detection of cardiotoxicity in patients

during and after cancer chemotherapy: a systematic review. J Am Coll Cardiol. 2014 Jul 1;63(25 Pt A):2751-68.

37. Russo C, Jin Z, Sera F, Lee ES, Homma S, Rundek T, Elkind MS, Sacco RL, Di Tullio MR. Left ventricular systolic dysfunction by longitudinal strain is an independent predictor of incident atrial fibrillation: a community-based cohort study. Circ Cardiovasc Imaging. 2015 Aug;8(8):e003520.

38. Korosoglou G, Gitsioudis G, Voss A, Lehrke S, Riedle N, Buss SJ, Zugck C, Giannitsis E, Osman NF, Katus HA. Strain-encoded cardiac magnetic resonance during high-dose dobutamine stress testing for the estimation of cardiac outcomes: comparison to clinical parameters and conventional wall motion readings. J Am Coll Cardiol. 2011 Sep 6;58(11):1140-9.

39. Buss SJ, Breuninger K, Lehrke S, Voss A, Galuschky C, Lossnitzer D, Andre F, Ehlermann P, Franke J, Taeger T, Frankenstein L, Steen H, Meder B, Giannitsis E, Katus HA, Korosoglou G. Assessment of myocardial deformation with cardiac magnetic resonance strain imaging improves risk stratification in patients with dilated cardiomyopathy. Eur Heart J Cardiovasc Imaging. 2015 Mar;16(3):307-15.

**Table 1.** The results of algorithm on the cardiac of XCAT phantoms and their reconstructed SPECT images

Gender	Age	Weight (kg)	Height (cm)	BMI	Φ	Θ	$\Phi_{(phantom)}$	$\Theta_{(phantom)}$
Male	36	87	176	24.38	35.05	59.35	38.34	62.09
Male	33	70	176	22.35	35.16	59.11	34.81	63.86
Male	67	89	178	28.22	35.08	57.87	38.08	60.70
Female	47	63	174	20.81	39.60	59.69	39.07	60.43

Table 2. Baseline characteristics of patients

	All patients (n=94)	Normal scan (n=53)	Abnormal scan (n=41)
Age (mean±SD)	65.65±10.04	67.15±10.03	63.71±9.83
Sex Male Female	 48 (51%) 46 (49%)	 24 (45%) 29 (55%)	 24 (58%) 17 (42%)
Θ (mean±SD)	101.44±35.84	78.86±24.68	130.62±25.44
Φ (mean±SD)	40.19±10.61	42.73±9.68	36.90±10.95
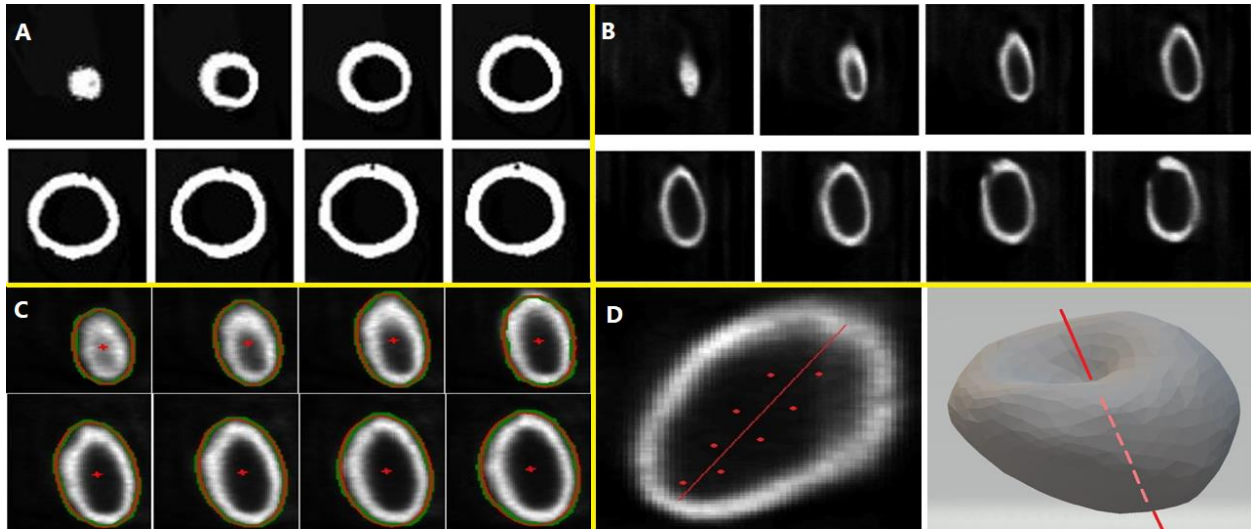
Fig 1. The short-axis view of cardiac of XCAT phantom (A) and its reconstructed SPECT (B). Estimated ellipse of heart in short-axis view (red dots are the center of the ellipse) (C) and estimated position of the left ventricular anatomical axis (LVAA) in the long axis view (D)
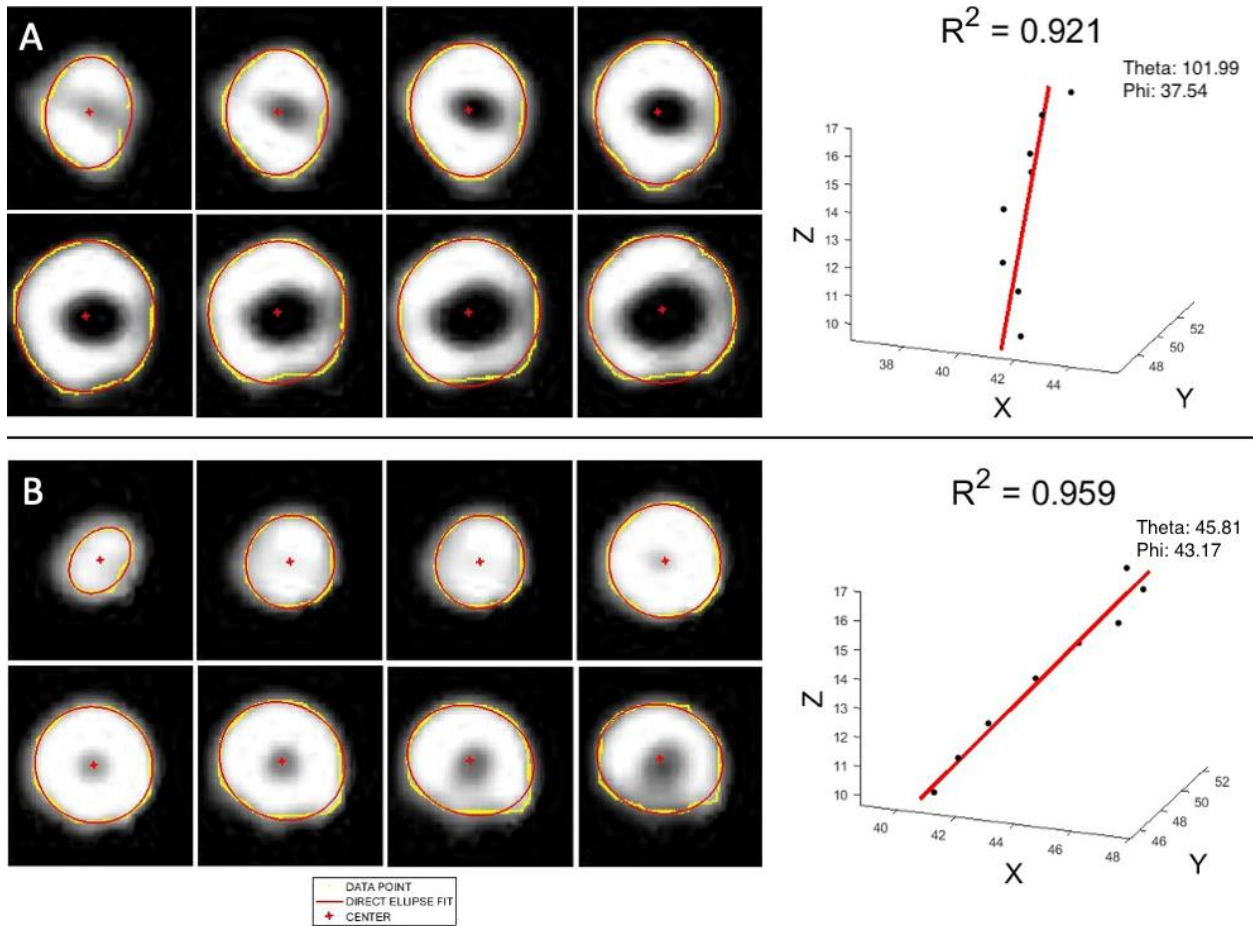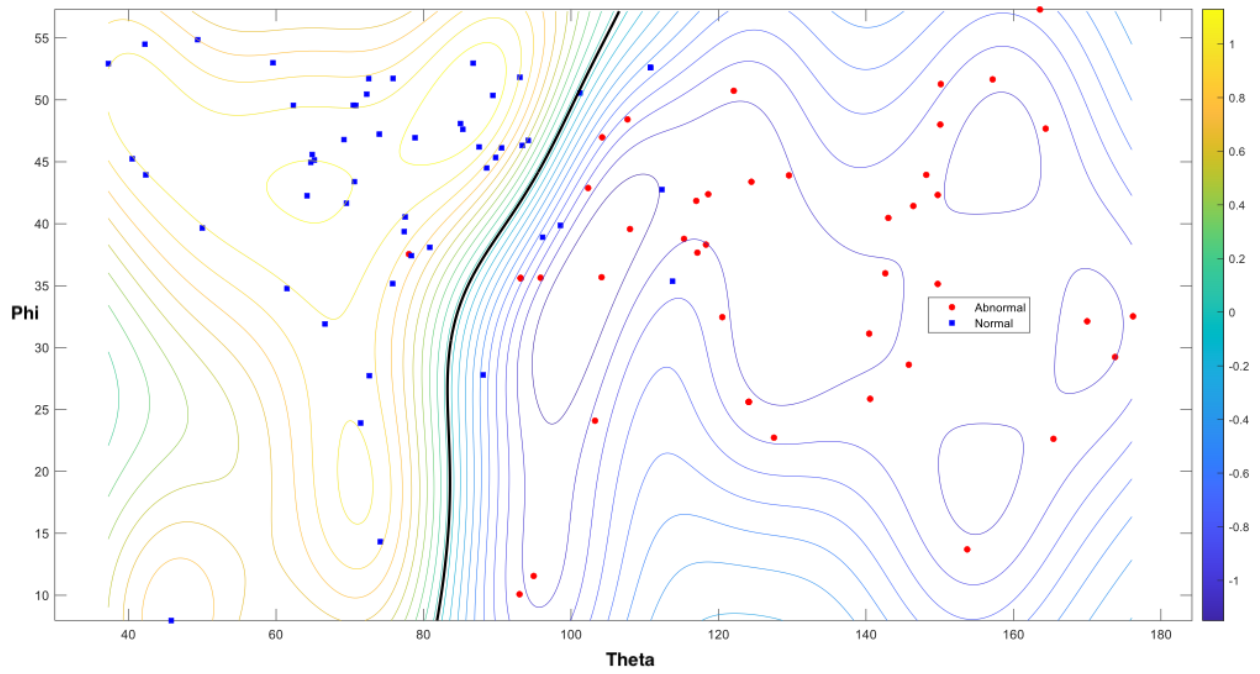
Fig 2. An example of image segmentation and achievement of the left ventricular anatomical axis (LVAA) with angles for an abnormal scan (A) and a normal scan (B)
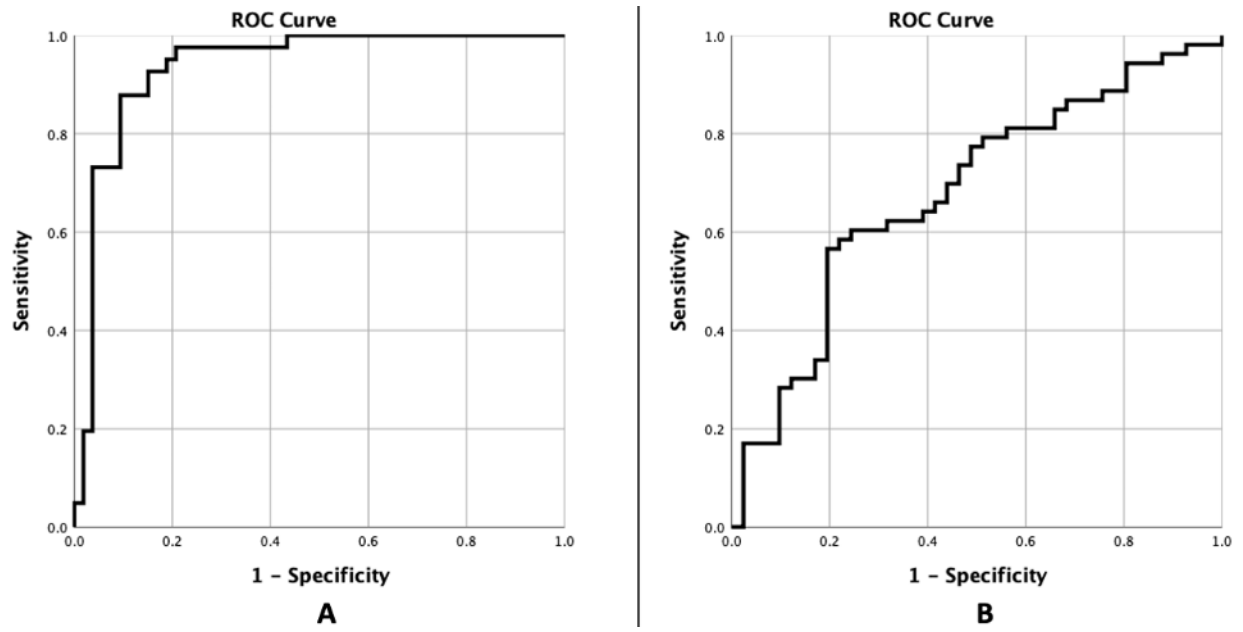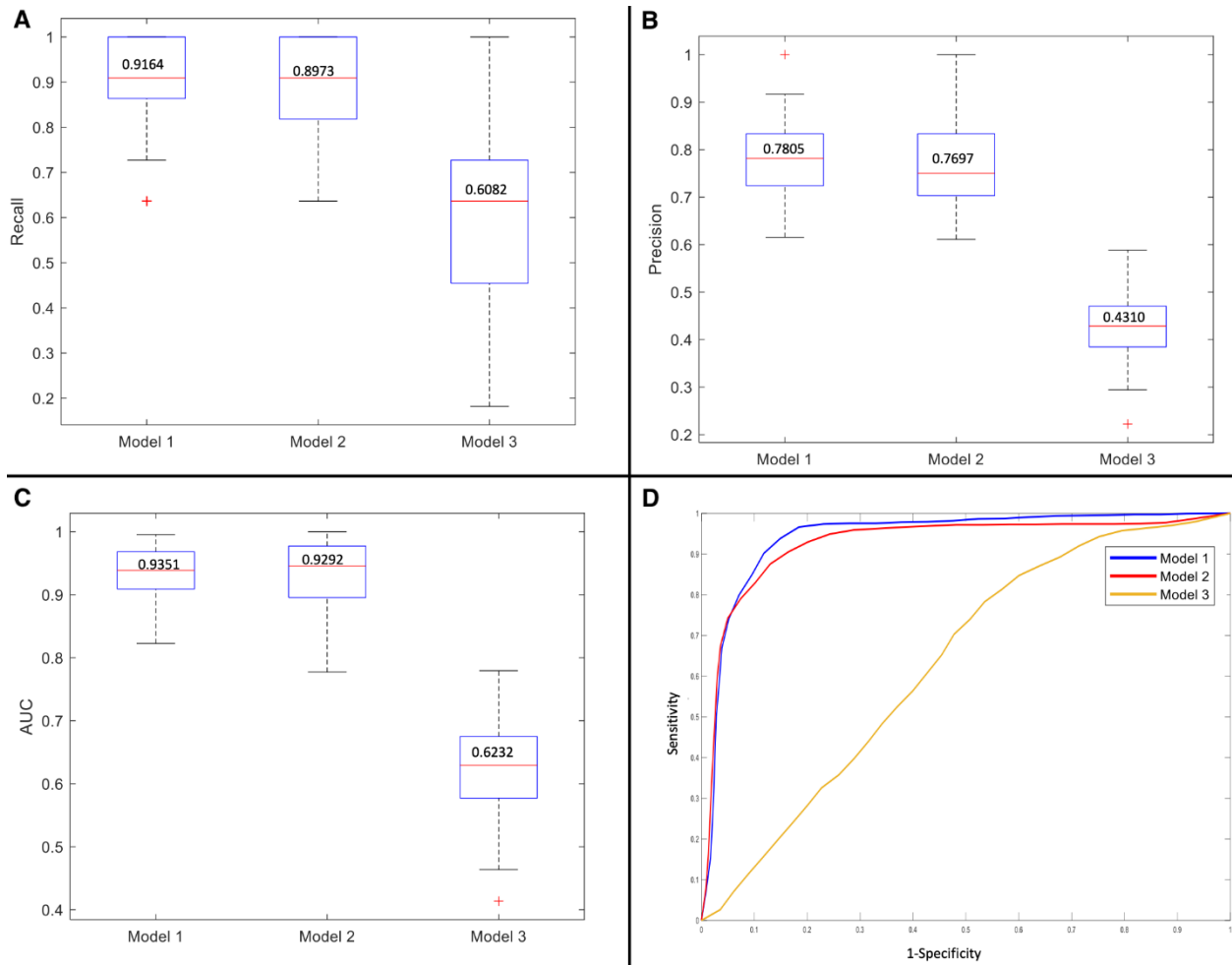
Fig 3. The receiver operating characteristic (ROC) curve of Θ (A) and Φ (B)

Fig 4. The results support vector machine (SVM) classification (whatever color of the lines moves to purple, that line is the boundary of classification)

Fig 5. The results of recall (A), precision (B), area under the curve (AUC) (C), and receiver operating characteristic (ROC) curve (D) for support vector machine (SVM) classification (model 1: Θ and Φ, model 2: Θ, model 3: Φ)